

Single-electron charging and detection in a laterally coupled quantum-dot circuit in the few-electron regime

L.-X. Zhang, P. Matagne, and J. P. Leburton

*Beckman Institute for Advanced Science & Technology and Department of Electrical and Computer Engineering,
University of Illinois at Urbana-Champaign, Urbana, Illinois 61801, USA*

R. Hanson and L. P. Kouwenhoven

*Department of NanoScience and ERATO Mesoscopic Correlation Project, Delft University of Technology, P.O. Box 5046,
2600 GA Delft, The Netherlands*

(Received 17 October 2003; revised manuscript received 22 December 2003; published 3 June 2004)

We provide a physical analysis of the charging and detection of the first few electrons in a laterally coupled GaAs/AlGaAs quantum-dot (LCQD) circuit with integrated quantum point contact read-out. Our analysis is based on the numerical solution of the Kohn-Sham equation incorporated into a three-dimensional self-consistent scheme for simulating the quantum device. Electronic states and eigenenergy spectra reflecting the particular LCQD confinement shape are obtained as a function of external gate voltages. We also derive the stability diagram for the first few electrons in the device, and obtain excellent agreement with experimental data.

DOI: 10.1103/PhysRevB.69.245301

PACS number(s): 73.21.-b, 72.20.My, 73.40.Gk

I. INTRODUCTION

Lateral GaAs/AlGaAs quantum dots (QD's) are now routinely fabricated with planar technology.¹ Three-dimensional (3D) quantum confinement is achieved, in part, by using the GaAs/AlGaAs semiconductor heterostructures to confine the conduction electrons into a two-dimensional electron gas (2DEG) at the interface between the two materials. By placing metal gates on top of such a structure, carrier confinement in other in-plane directions can be realized by energizing the gates that create lateral energy barriers to electrons in the 2DEG. Design of these QD's, which previously contained tens of electrons, has been improved to operate them in a few-electron regime where the charging of the very first electrons can be observed experimentally.² Two quantum dots can be placed adjacent to each other to form a laterally coupled device with both electrostatic and quantum-mechanical coupling between them.^{3,4} Fine variations of the top gate biases change the confinement of each dot, while precise coupling between them through the central gates leads to a fully tunable two-qubit quantum system, which can be used as a building block for quantum computing.⁵

Recently, it has been shown that laterally coupled quantum dots (LCQD) containing a few conduction electrons could be coupled to single charge detectors to form an integrated quantum circuit.⁴ The read-out of the charge state in the LCQD is realized by integrating monolithically quantum point contacts (QPC's) adjacent to each of the QD's. Each QPC can be calibrated through electrostatic coupling with the dots so that its conductivity changes abruptly once a single-electron charging event occurs in one of the dots.^{6,7} With this sensitive detector, it is then possible to obtain the "stability diagram" that describes the stable charge regimes of the LCQD as a function of the tuning (plunger) gate biases.^{8,9}

This quantum-dot circuit has a two fold advantage: it is possible (i) to scale it to a quantum-dot array, and (ii) to

perform single-quantum sensitivity measurements, both of which are favorable features of a realizable quantum computer.¹⁰

In this paper, we study the properties of the above circuit via numerical simulation that involves the self-consistent solution of coupled Poisson and Kohn-Sham equations discretized on a 3D mesh.^{11,13} In Sec. II we describe the LCQD structure and in Sec. III we present the approach for solving the Kohn-Sham equations in the device environment within the local spin-density approximation (LSDA) and express the criterion used to determine the charging events as a function of the applied gate biases. In Sec. IV we present our simulation results of the circuit, including both electrostatic and quantum-mechanical features, the functionality of the QPC's, and the stability diagram in the few-electron charging regime. Finally, we summarize our work in Sec. V.

II. DOT STRUCTURES

Figure 1(a) shows the top view of the LCQD and QPC gates in the xy plane.⁴ Top L, R, T, and M gates are used to define the coupled-dot region. Among them, the T and M gates can also control the coupling between the two dots. The PL and PR gates, called the "plungers," have smaller feature sizes than the other gates and are used for fine tuning the confinement of each dot. The QPC-L and QPC-R gates are associated with the L and R gates (via the tips) to form the QPC detectors. Charging paths into the dots (shown by the ovals) from external reservoirs are shown by curved arrows, whereas the QPC currents are shown by straight arrows. Figure 1(b) shows a cross-sectional view of the layer structure in the z direction. Our model involves four different layers of semiconductor materials (from top to bottom): a 50 Å thick n -type ($N_D = 1.5 \times 10^{18} \text{ cm}^{-3}$) GaAs layer, a 650 Å thick n -type ($N_D = 0.31 \times 10^{18} \text{ cm}^{-3}$) Al_{0.27}Ga_{0.73}As layer, a 200 Å thick undoped Al_{0.27}Ga_{0.73}As layer, and a 1610 nm thick p -type ($N_A = 1.0 \times 10^{15} \text{ cm}^{-3}$) GaAs layer. The 2DEG

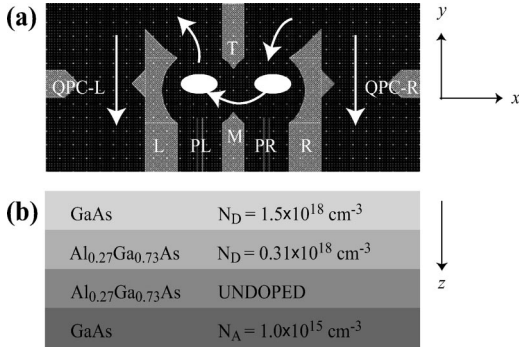


FIG. 1. (a) Layout of the top gates (light gray areas show the gate pattern for the LCQD and the QPC's; ovals show the dots; curved arrows show the possible charging current paths; and straight arrows show the QPC currents). (b) Layers of the heterostructure (not to scale), after Elzerman *et al.* (Ref. 4).

is formed at the interface between the undoped AlGaAs layer and the lightly p -type doped GaAs layer (900 Å below the top surface).

III. NUMERICAL MODEL

The electron density in the LCQD region is obtained by describing the charge carriers within the density-functional theory that incorporates many-body effects among particles.^{14,15} In order to take into account the spin dependence of the electron-electron interaction, the Kohn-Sham equations¹⁶ for spin up (\uparrow) and spin down (\downarrow) are solved simultaneously:

$$H^\uparrow \psi_i^\uparrow(\mathbf{r}) = \varepsilon_i^\uparrow \psi_i^\uparrow(\mathbf{r}), \quad H^\downarrow \psi_i^\downarrow(\mathbf{r}) = \varepsilon_i^\downarrow \psi_i^\downarrow(\mathbf{r}). \quad (1)$$

Here, $\varepsilon_i^{\uparrow(\downarrow)}$ and $\psi_i^{\uparrow(\downarrow)}$ are the corresponding eigenenergies and eigenfunctions of the Hamiltonian $H^{\uparrow(\downarrow)}$:

$$H^{\uparrow(\downarrow)} = -\frac{\hbar^2}{2} \nabla \left[\frac{1}{m^*(\mathbf{r})} \nabla \right] - q\phi(\mathbf{r}) + \Delta E_c + \phi_{xc}^{\uparrow(\downarrow)}(n), \quad (2)$$

where $m^*(\mathbf{r})$ is the position dependent effective mass. $\phi(\mathbf{r}) = \phi_{ext} + \phi_{ion} + \phi_H$ is the electrostatic potential which consists of three parts: ϕ_{ext} is the potential due to external gate biases; ϕ_{ion} is the potential resulting from ionized donors and acceptors; and ϕ_H is the Hartree potential accounting for repulsive electron-electron interactions. ΔE_c is the conduction-band offset between different materials, and $\phi_{xc}^{\uparrow(\downarrow)}(\mathbf{r})$ is the exchange-correlation potential energy for spin up (\uparrow) and spin down (\downarrow) computed within the LSDA according to Perdew and Wang's formulation.¹⁷ Hence our approach is spin unrestricted by allowing different orbitals with different spins.

The electron density $n(\mathbf{r})$ in the LCQD region is

$$n(\mathbf{r}) = n^\uparrow(\mathbf{r}) + n^\downarrow(\mathbf{r}) = \sum_{i=1}^{N_\uparrow} |\psi_i^\uparrow(\mathbf{r})|^2 + \sum_{i=1}^{N_\downarrow} |\psi_i^\downarrow(\mathbf{r})|^2, \quad (3)$$

where $N_\uparrow + N_\downarrow = N$ is the total number of electrons in the dots.

The electrostatic potential $\phi(\mathbf{r})$ is computed by solving Poisson's equation,

$$\nabla[\epsilon(\mathbf{r})\nabla\phi(\mathbf{r})] = -\rho(\mathbf{r}), \quad (4)$$

where $\epsilon(\mathbf{r})$ is the position-dependent permittivity and $\rho(\mathbf{r})$ is the total charge density given by

$$\rho(\mathbf{r}) = q[N_D^+(\mathbf{r}) - N_A^-(\mathbf{r}) + p(\mathbf{r}) - n(\mathbf{r})]. \quad (5)$$

Here, $N_D^+(\mathbf{r})$ and $N_A^-(\mathbf{r})$ are the ionized donor and acceptor concentrations in the relevant device layers; $p(\mathbf{r})$ is the hole concentration; and $n(\mathbf{r})$ is the total electron concentration given by Eq. (3) in the QD region, while outside this region the free electron charge is entirely determined by using the semiclassical Thomas-Fermi approximation.¹³

We solve 3D Kohn-Sham and Poisson equations self-consistently by the finite element method.^{11,13} Zero normal electric field on lateral and bottom surfaces, and Schottky barrier values ($-q\phi_s = -q\phi_s^0 - qV_G$, where $\phi_s^0 = -0.8$ V, and V_G is the applied gate bias) on the top surface under the gates are imposed as boundary conditions for the solution of Poisson's equation. We use the same boundary conditions but with $V_G = 0$ on the top exposed surfaces.^{12,13} Since the quantum dots are much smaller than the physical dimension of the device, the wave functions actually vanish long before reaching the device boundaries. This allows us to embed a local region in the global mesh for solving the Kohn-Sham equations. This local region is chosen large enough to ensure vanishing wave functions on its boundaries. A nonuniform 3D grid of 141, 52, and 71 mesh points in the x , y , and z directions, respectively, is used for solving Poisson's equation, while $71 \times 45 \times 19$ grid points are used to discretize the local region where the Kohn-Sham wave functions are evaluated.

Because the LCQD are weakly coupled to the external reservoirs, we assume that electrons in the dots are completely localized in that region. At equilibrium, and for a given bias, an integer number of electrons N minimizes the total energy E_T of the dots. In order to determine N , we use the Slater formula:¹⁸

$$E_T(N+1) - E_T(N) = \int_0^1 \varepsilon_{LUO}(n) dn \approx \varepsilon_{LUO}(1/2) - E_F, \quad (6)$$

where $E_T(N+1)[E_T(N)]$ is the total energy for $N+1$ (N) electrons in the dots, and $\varepsilon_{LUO}(1/2)$ is the eigenenergy of "the lowest unoccupied orbital" with half occupancy. The sign change of the right-hand side of Eq. (6), as a function of the tuning gate voltage, determines the electron occupation in the LCQD. In our simulation, we use a variation of the above rule where charging occurs when $\varepsilon_{LUO}(1) - E_F = E_F - \varepsilon_{LUO}(0)$, which was justified in Ref. 13.

IV. RESULTS AND DISCUSSIONS

Figure 2 shows the conduction-band edge profiles in the xy plane at the 2DEG interface [contour plot, Fig. 2(a)] and in the z direction [Fig. 2(b)] under the condition $V_L = V_R = V_{QPC-L} = V_{QPC-R} = V_M = -0.585$ V, $V_T = -0.9$ V, V_{PL}

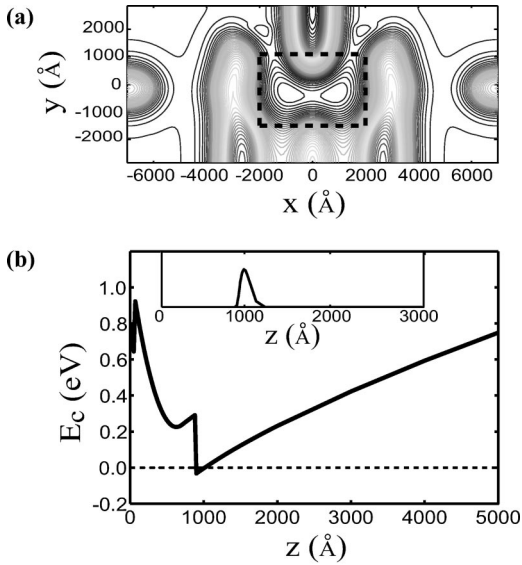


FIG. 2. Conduction-band edge profile in the LCQD-QPC structure: (a) contour plot in the xy plane at the 2DEG interface (the dashed rectangle shows the location of the dots), (b) along the z direction with the inset showing the shape of the ground-state wave function ($V_{PL}=V_{PR}=-0.15$ V, zero electrons in the LCQD).

$=V_{PR}=-0.15$ V (these voltages correspond to point A in Fig. 7) and zero electrons in the dots. The Fermi level is set at zero throughout the device at the temperature $T=4$ K. The LCQD region and the QPC region with low equipotential line density are clearly visible in Fig. 2(a). The outer energy barrier for the LCQD is ~ 110 meV whereas the energy barrier between the dots is ~ 9 meV. A large negative T gate bias is used to prevent the wave functions from leaking into the external reservoirs, which clearly defines the LCQD region. Also, clearly visible are the QPC constrictions in the potential at $x \sim \pm 4900$ Å and $y \sim 0$ Å. The confinement along the z direction is achieved by a quasitriangular shaped well shown in Fig. 2(b), for which the relaxation of the potential to zero field is not shown at the far end (substrate) of the device. Due to the strong confinement in the triangular well, only the ground state along the z direction is occupied [the shape of the ground-state wave function along the z direction is shown in the inset in Fig. 2(b)]. Under the above condition, the wave function contour plots in the xy plane at the 2DEG interface are shown in ascending energies for the first eight spin-up (\uparrow) eigenstates in Fig. 3. A similar set of wave functions is obtained for the spin-down (\downarrow) eigenstates (not shown). They are similar to orbitals observed in diatomic molecules: the two columns represent the familiar bonding and antibonding state pairs. Notice that the shape of the wave functions reflects the shape of the confinement seen in the local minima of the conduction-band edge in Fig. 2(a).

In Fig. 4(a), we show the variation of the first eight spin-up (\uparrow) eigenenergies when the plunger gate bias configuration is changed from the values $V_{PL}=V_{PR}=-0.15$ V to the new values $V_{PL}=-0.15$ V, $V_{PR}=-0.06$ V. On the stability diagram (Fig. 7), this transition is represented on the vertical A to B line by the diamond indicating the charging point for the first electron. The first eight eigenenergies are

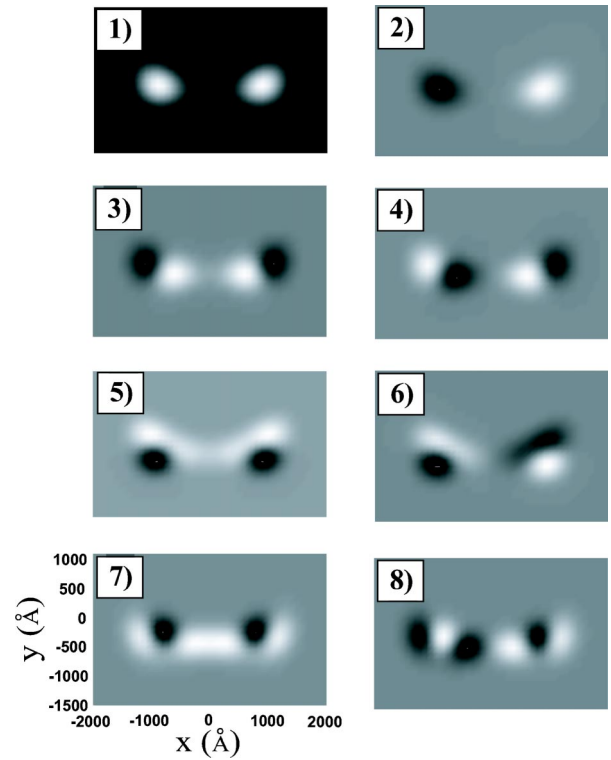


FIG. 3. Contour plot of the first eight spin-up (\uparrow) eigenstates in ascending energies in the xy plane at the 2DEG interface with zero electrons in the LCQD ($V_{PL}=V_{PR}=-0.15$ V). The xy coordinates are given for the lower left wave function, which is a zoom-in region corresponding to the dashed rectangular region in Fig. 2(a). All the other wave function contour plots in this paper are on the same scale.

separated into two groups, one for the right dot (solid lines) and one for the left dot (dashed lines), which are lowered simultaneously as the right plunger gate bias increases. However, the eigenenergies of the right dot decrease more rapidly than those of the left dot because of the proximity of the former to the varying plunger. At $V_{PR}=-0.074$ V, the charging of the first electron [spin up (\uparrow)] occurs in the right dot, which is indicated by a discontinuity of 8.2×10^{-4} eV in the variation of the ground-state energy level with respect to the right plunger gate bias. At the same gate bias, we also observe a jump of the conduction band edge in the constriction of the two QPC's, i.e., 2.6×10^{-6} eV for the left QPC and 5.4×10^{-6} eV for the right QPC [see Fig. 4(b), where the vertical axis is shifted up by 0.0201 eV for clarity]. The upshift of the conduction-band edge in the QPC constriction results from the Coulomb interaction between the electrons in the LCQD and electrons in the QPC's, which reduces the total charge number in the conduction channel and leads to a discontinuity in the QPC current observed in experiments.⁴ Obviously, the right QPC is more sensitive to the single-electron charging because of its proximity with the right dot. From the discontinuity value in the conduction-band edge, we can estimate the variation of the QPC conductance during the transition toward the first quantized plateau $G_0=2e^2/h$ to be $\delta G/G=1.7\%$ for the right QPC with $\hbar\omega_y \sim 1$ meV obtained from the simulation (see the Appendix), which is of

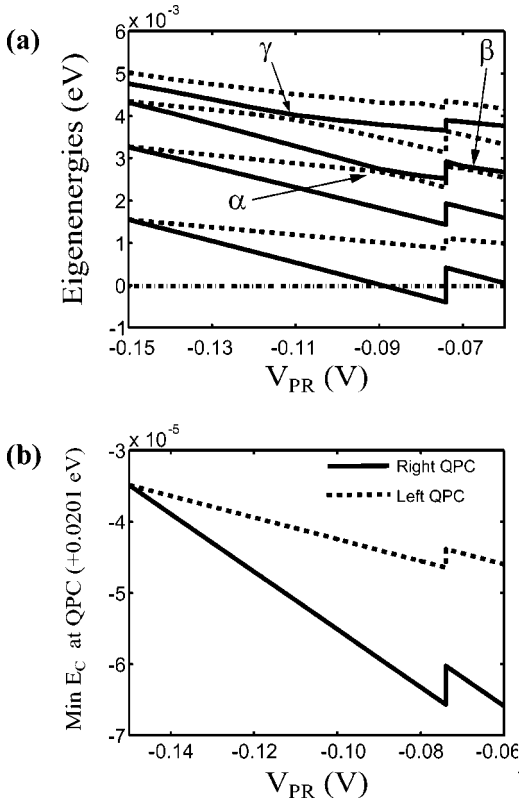


FIG. 4. (a) Eigenenergy spectrum [spin-up (\uparrow) states] as a function of the right plunger gate bias (solid lines: right dot; dashed lines: left dot). α , β and γ are three anticrossing points. (b) Variation of the conduction-band edge in the constriction of the left and right QPC's as a function of the right plunger gate bias from point A to B in Fig. 7 [V_{PL} is fixed to -0.15 V; the vertical axis of Fig. 4(b) is shifted up by 0.0201 eV].

the same order of magnitude as found experimentally.⁴

From the eigenenergies variation versus V_{PR} diagram [Fig. 4(a)], we also observe three “anticrossing” points between the two different sets of eigenenergy levels, each arising from the distinct QD's as mentioned above and indicated by arrows in Fig. 4(a), i.e., (α) at $V_{PR} \sim -0.09$ V, between the third and fourth excited states; (β) at $V_{PR} \sim -0.07$ V, between the third and fourth excited states; and (γ) at $V_{PR} \sim -0.11$ V, between the fifth and sixth excited states. The behavior of the system near the anticrossing points can be further illustrated by examining the evolution of the wave functions for the anticrossing levels. “Interchange” of the wave functions is clearly observed before and after these points. In Fig. 5, contour plots of the wave functions in the xy plane at the 2DEG interface are shown for the three anticrossing points: the third and fourth excited states labeled α_1 , α_2 at $V_{PR} = -0.10$ V and α'_1 , α'_2 at $V_{PR} = -0.08$ V, respectively; the third and fourth excited states labeled β_1 , β_2 at $V_{PR} = -0.074$ V and β'_1 , β'_2 at $V_{PR} = -0.06$ V; and the fifth and sixth excited states labeled γ_1 , γ_2 at $V_{PR} = -0.12$ V and γ'_1 , γ'_2 at $V_{PR} = -0.10$ V.

The detection of single-electron charging events can also be carried out for the B to C transition in Fig. 7, in which the right plunger gate bias V_{PR} is fixed to be -0.06 V while the

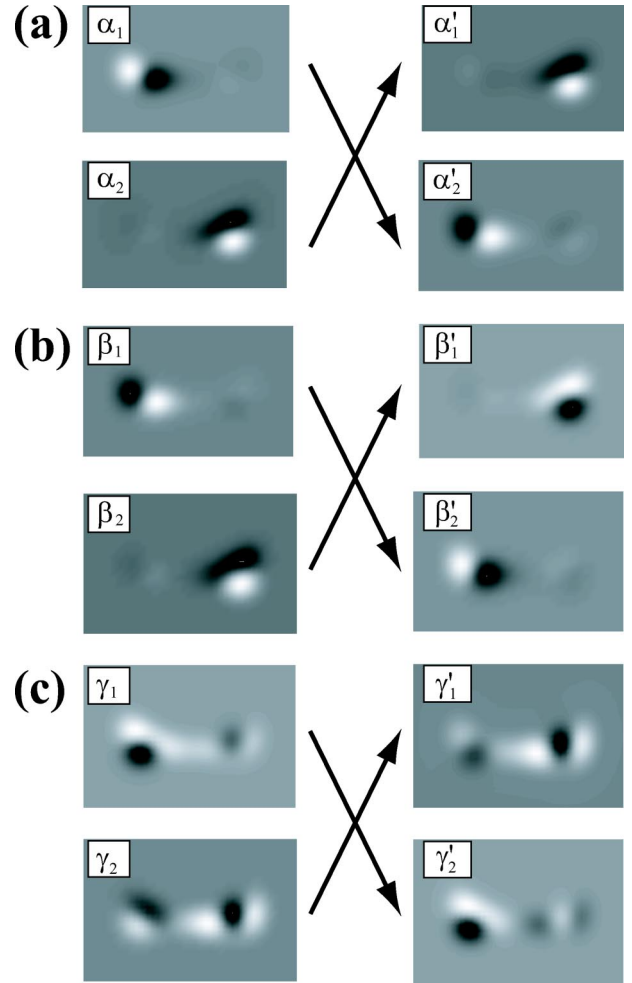


FIG. 5. Wave function [for spin-up (\uparrow) states] interchanges at the anticrossing points corresponding to (a) point α , (b) point β , and (c) point γ in Fig. 4(a).

left plunger gate bias is changed from $V_{PL} = -0.15$ V to $V_{PL} = -0.06$ V. The variation of the spin-up (\uparrow) eigenenergies with respect to the Fermi level and the conduction-band edge in the constriction of the two QPC's are shown in Figs. 6(a) and 6(b), respectively. In this case, the transition of the charging state is from one electron in the right dot to two electrons, one in each dot occupying an individual 1S-like orbital,¹⁹ and occurs when the left plunger gate bias V_{PL} is at -0.097 V. The charging of the second electron into the system is localized in the left dot and is indicated by the jump of the first excited state energy level. Note that in this case, the variation of eigenenergies in the left QD (dashed lines) is larger than those in the right dot (solid lines). In our LSDA approach, the second electron has the same spin [spin up (\uparrow)] as the first one as they are uncorrelated by the height of the coupling barrier. The corresponding jump of the conduction-band edge is 5.6×10^{-6} eV for the left QPC and 2.8×10^{-6} eV for the right one. The left QPC is more sensitive to the second electron charging because it occurs in the left dot.

Following the same procedure as described above, we can find another charging path for the first electron charging, i.e.,

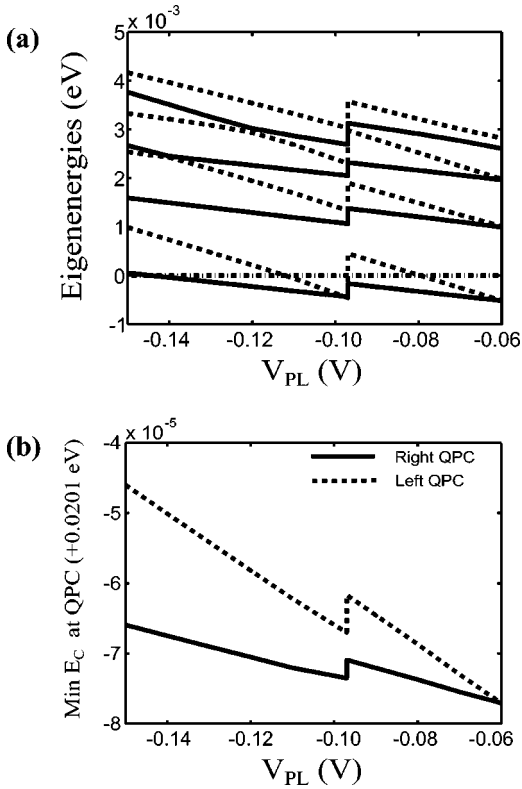


FIG. 6. (a) Eigenenergy spectrum [spin-up (\uparrow) states] (solid lines: right dot; dashed lines: left dot) and (b) variation of the conduction-band edge in the constriction of the left and right QPC's as a function of the left plunger gate bias from point *B* to *C* in Fig. 7 [V_{PR} is fixed to -0.06 V; the vertical axis of Fig. 6(b) is shifted up by 0.0201 eV].

from point *E* to *F* in Fig. 7, and for the charging from one to two electrons, *F* to *G* in Fig. 7, for distinct stable charge regimes of electrons in the two dots. On the path *E* to *F* (V_{PL} is fixed to -0.125 V, V_{PR} is changed from -0.125 V to -0.07 V), charging occurs for the first electron [spin up (\uparrow)] in the right dot at $V_{PR} = -0.082$ V; on the path *F* to *G* (V_{PR} is fixed to -0.07 V, V_{PL} is changed from -0.125 V to -0.07 V), charging occurs for the second electron [spin up (\uparrow)] in the left dot at $V_{PL} = -0.092$ V.

We can further interchange the plunger gate biases and obtain different transitions, i.e., from *A* to *D* to *C* and *E* to *H* to *G*, as shown in Fig. 7 to realize closed cycles of charging and discharging paths. These two closed paths (dashed and dotted lines) are shown in Fig. 7. Each corner of the two squares is in a different stable charge state with numbers in the parentheses showing the electron number in the left and right dots, respectively, e.g., (0,1) means zero electrons in the left dot and one in the right dot. On each path, we record the charging points (diamonds in Fig. 7) and make linear extrapolations between the two charging points on each of the two parallel paths, which leads to four lines crossing at two points (circles in Fig. 7).

The two crossing points are linked afterwards. Now, five segments (solid lines in Fig. 7) separate the diagram into four regions to define the stability diagram for the LCQD system in the few-electron charging regime. Each region, separated

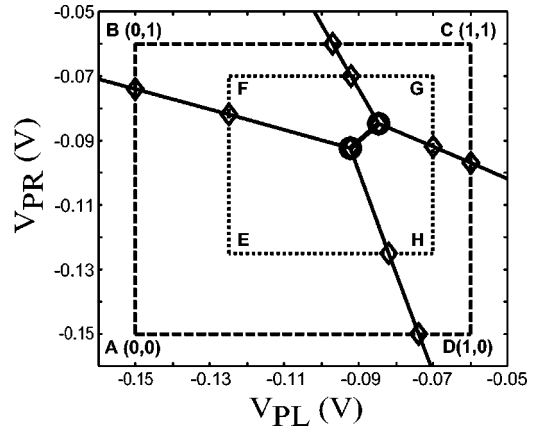


FIG. 7. Stability diagram for the first two charging electrons characterizing the double-triple point (shown by circles).

by the solid lines, indicates a stable charge configuration assumed by the LCQD under a particular range of plunger gate biases. More interesting are the two crossing points (circles), called the double-triple point,⁹ occurring at $V_{PL} = V_{PR} = -0.0924$ V for the three charging states (0,0), (0,1), and (1,0) and at $V_{PL} = V_{PR} = -0.0847$ V for (0,1), (1,0), and (1,1) states. We then determine the voltage range of the right plunger that spans the distance between the double-triple point to be $\Delta V_{PR} = 7.7$ mV, which is comparable to the experimental result ~ 7.4 mV.⁴

Finally, from the charging diagrams in the few-electron regime we extract the addition energy for the second electron charging in the right dot: we determine the V_{PR} -voltage interval on the stability diagram for the (0,1) configuration [i.e., between the (0,0) configuration and the (0,2) configuration in the singlet state] to be 0.1 V, which is in excellent agreement with the experimental result ~ 0.1 V.⁴ By linear projection of this V_{PR} interval to the energy scale,¹³ we obtain then the addition energy for charging the second electron, which is 2.5 meV. By comparing this value to the experimental result of 3.7 meV,⁴ we attribute the difference to the fact that our simulation is performed on a coupled-dot system, while the experimental result is obtained by grounding one of the dots where the confinement is stronger in an individual dot compared to our simulation case.

V. CONCLUSION

We performed numerical simulations of the electrostatic and quantum-mechanical characteristics of a laterally coupled quantum-dot circuit with integrated quantum point contact read-out. We were able to reproduce detailed single-electron charging behavior of the elementary quantum circuit and estimate the quantum point contact conductance sensitivity to the single-electron charging. In particular, we obtained excellent agreement with the experiment for the voltage range of the extension of the double-triple point at the (0,0) to (1,1) transition and the addition energy for single-electron charging in the dots, which validates our quantum device modeling approach for simulating efficiently nanoscale qubit circuits.

ACKNOWLEDGMENTS

This work was supported by DARPA QUIST program through ARO Grant DAAD 19-01-1-0659. The authors thank D. Melnikov for constructive discussions. L.-X. Zhang thanks R. Ravishankar and S. Barraza-Lopez for their technical assistance.

APPENDIX

We follow Büttiker,²⁰ and write the conductance through the QPC as

$$G = G_0 T, \quad (\text{A1})$$

where $G_0 = 2e^2/h$, $T = 1/(1 + e^{-\pi\epsilon_0})$, and $\epsilon_0 = (2E - \hbar\omega_x - 2E_c^0)/\hbar\omega_y$. Here, E_c^0 is the potential energy E_c at the saddle point in the QPC constriction and the curvatures of E_c along the x and y directions are expressed in terms of the

frequencies ω_x and ω_y . In the linear response approximation,

$$\delta G = G_0 \frac{\partial T}{\partial E_c^0} \delta E_c^0, \quad (\text{A2})$$

where

$$\frac{\partial T}{\partial E_c^0} = \frac{-2\pi/\hbar\omega_y}{(1 + e^{-\pi\epsilon_0})^2} e^{-\pi\epsilon_0}. \quad (\text{A3})$$

We find

$$\frac{\delta G}{G} = -\frac{\pi}{\hbar\omega_y} \delta E_c^0 \quad (\text{A4})$$

at $G = G_0/2$, i.e., $\epsilon_0 = 0$, while noting that δE_c^0 is weakly sensitive to the ϵ_0 variation.

¹M.A. Kastner, Rev. Mod. Phys. **64**, 849 (1992).

²M. Ciorga, A.S. Sachrajda, P. Hawrylak, C. Gould, P. Zawadzki, S. Jullian, Y. Feng, and Z. Wasilewski, Phys. Rev. B **61**, R16 315 (2000).

³F.R. Waugh, M.J. Berry, D.J. Mar, R.M. Westervelt, K.L. Campman, and A.C. Gossard, Phys. Rev. Lett. **75**, 705 (1995).

⁴J.M. Elzerman, R. Hanson, J.S. Geidanus, L.H. Willems Van Beveren, S. De Franceschi, L.M.K. Vandersypen, S. Tarucha, and L.P. Kouwenhoven, Phys. Rev. B **67**, 161308(R) (2003).

⁵D. Loss and D.P. DiVincenzo, Phys. Rev. A **57**, 120 (1998).

⁶M. Field, C.G. Smith, M. Pepper, D.A. Ritchie, J.E.F. Frost, G.A.C. Jones, and D.G. Hasko, Phys. Rev. Lett. **70**, 1311 (1993).

⁷D. Sprinzak, Y. Ji, M. Heiblum, D. Mahalu, and H. Shtrikman, Phys. Rev. Lett. **88**, 176805 (2002).

⁸H. Pothier, P. Lafarge, C. Urbina, D. Esteve, and M.H. Devoret, Europhys. Lett. **17**, 249 (1992).

⁹W.G. van der Wiel, S. De Franceschi, J.M. Elzerman, T. Fujisawa,

S. Tarucha, and L.P. Kouwenhoven, Rev. Mod. Phys. **75**, 1 (2003).

¹⁰C.H. Bennett and D.P. DiVincenzo, Nature (London) **404**, 247 (2000).

¹¹P. Matagne, J.-P. Leburton, J. Destine, and G. Cantraine, Comp. Mod. Eng. Sciences **1**, 1 (2000).

¹²D. Jovanovic and J.-P. Leburton, Phys. Rev. B **49**, 7474 (1994).

¹³P. Matagne and J.-P. Leburton, Phys. Rev. B **65**, 235323 (2002).

¹⁴R.O. Jones and O. Gunnarsson, Rev. Mod. Phys. **61**, 689 (1989).

¹⁵S.M. Reimann and M. Manninen, Rev. Mod. Phys. **74**, 1283 (2002).

¹⁶W. Kohn and L.J. Sham, Phys. Rev. **140**, A1133 (1965).

¹⁷J.P. Perdew and Y. Wang, Phys. Rev. B **45**, 13 244 (1992).

¹⁸J.C. Slater, Adv. Quantum Chem. **6**, 1 (1972).

¹⁹S. Nagaraja, J.-P. Leburton, and R.M. Martin, Phys. Rev. B **60**, 8759 (1999).

²⁰M. Büttiker, Phys. Rev. B **41**, 7906 (1990).